Smart Structures and Systems, *Vol. 28, No. 1 (2021) 55-67*
https://doi.org/10.12989/sss.2021.28.1.055

Debonding defect quantification method of building decoration layers via UAV-thermography and deep learning

Xiong Peng [1b], Xingu Zhong*[2a], Anhua Chen [1a], Chao Zhao [2a], Canlong Liu [1b] and Y. Frank Chen [3a]

[1] *Hunan University of Science and Technology, Taoyuan Road, Yuhu District, Xiangtan, China*
[2] *Hunan Provincial Key Laboratory of Structures for Wind Resistance and Vibration Control*
& School of Civil Engineering, Hunan University of Science and Technology, Taoyuan Road, Yuhu District, Xiangtan, China
[3] *Department of Civil Engineering, Pennsylvania State University, Middletown, PA, USA*

(*Received April 27, 2020, Revised March 20, 2021, Accepted March 30, 2021*)

Abstract. The falling offs of building decorative layers (BDLs) on exterior walls are quite common, especially in Asia, which presents great concerns to human safety and properties. Presently, there is no effective technique to detect the debonding of the exterior finish because debonding are hidden defect. In this study, the debonding defect identification method of building decoration layers via UAV-thermography and deep learning is proposed. Firstly, the temperature field characteristics of debonding defects are tested and analyzed, showing that it is feasible to identify the debonding of BDLs based on UAV. Then, a debonding defect recognition and quantification method combining CenterNet (Point Network) and fuzzy clustering is proposed. Further, the actual area of debonding defect is quantified through the optical imaging principle using the real-time measured distance. Finally, a case study of the old teaching-building inspection is carried out to demonstrate the effectiveness of the proposed method, showing that the proposed model performs well with an accuracy above 90%, which is valuable to the society.

Keywords: building decorative layers; debonding defect; deep learning; infrared thermography; UAV

1. Introduction

Materials like ceramics, concrete, and pebbles are commonly used for the building decoration layers (BDLs) on exterior walls (Feng and Wang 2014). Due to the problems of localized voids and low material strength during construction, debonding of BDLs will occur and aggravate under the natural environmental conditions, such as rain erosion, repeated freeze-thaws, and daily and seasonal temperature variations, shown in Fig. 1(a) (Zhu *et al*. 2016). Traditionally, the debonding defect detection method of BDLs is conducted manually shown in Fig. 2(b) by setting up some kinds of brackets outside of the exterior wall, which is time-consuming, unsafe, and unreliable. Therefore, it is necessary to come up with an effective method to identify the debonding defect locations and areas and further to take corresponding measures to prevent possible accidents.

Previous studies (Zhu *et al*. 2016) have shown that there is a difference in energy emission between the surface and the inside of debonding concrete duo to the change of atmospheric temperatures. It has also been found feasible to obtain the infrared thermal images of hidden defect, thereby identifying the gray scale feature and recognizing the defect locations and areas indirectly. To be specific, Pitarma *et al*. (2019) inspected the inside wood damage using infrared thermography. Cotič *et al*. (2015) studied the detection method for void defects of concrete based on infrared thermal image with an accuracy of above 90%. Rocha *et al*. (2019) detected the delamination with different thicknesses (3, 6 and 12 mm) and depths (25, 50 and 75 mm) in sunlight-unexposed concrete elements of bridges using infrared thermography. Bang *et al*. (2020) proposed defect identification method in composite materials via thermography. Hwang *et al*. (2020) inspected internal delamination in wind turbine blades using continuous line laser scanning thermography.

However, most of the thermography methods mentioned here are fixed in the ground resulting in a relatively restricted elevation range (0~45). Meanwhile, the pixel resolution of thermography imaging is limited (≦ 1280 × 1024 pixels) (Sirca and Adeli 2018). As shown in Fig. 2(a),

Fig. 1 Debonding defects of BDLs

---

*Corresponding author, Ph.D.,
E-mail: 1020086@hnust.edu.cn
[a] Ph.D.
[b] Ph.D. Student

ISSN: 1738-1584 (Print), 1738-1991 (Online)

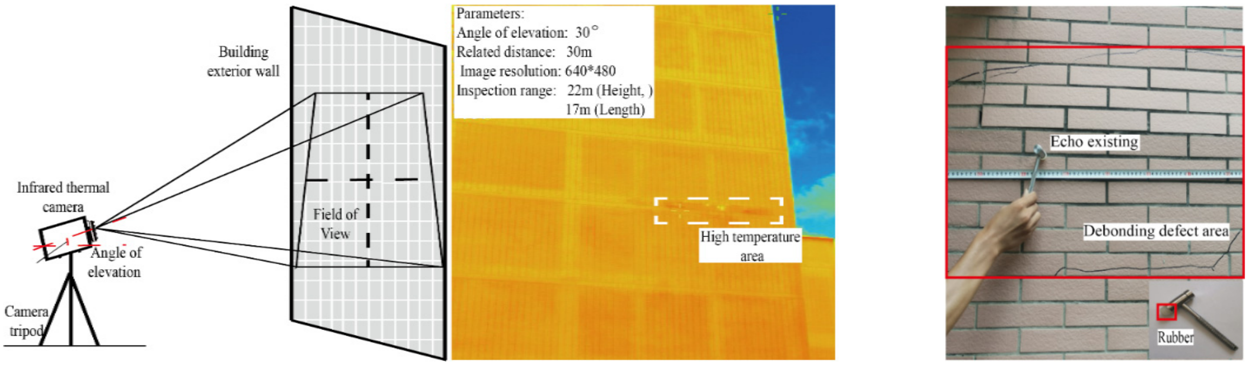

(a) Debonding defect measurement fixed on-ground (b) Traditional manual detection method

Fig. 2 Traditional debonding defect detection

the range (height 22 m, length 17 m) of debonding defect inspection is limited by the elevation angle and pixel resolution, which is impossible to find the debonding defect of BDLs on mid- and high-rise buildings by ground-fixed thermography imaging.

In recent years, the unmanned aerial vehicle (UAV) has been rapidly applied to civil structures (Liu *et al*. 2014, Kim *et al*. 2017, Zhong *et al*. 2018, Jung *et al*. 2019, Özcan and Özcan 2021, Jang *et al*. 2021), which is a good alternative tool for detecting debonding defects of BDLs in conjunction with the use of infrared thermal imaging. Utilizing UAVs offers several advantages, including no need of brackets, unlimited space, fast speed, and cost savings in infrared thermal imaging. Specifically, Ellenberg *et al*. (2016) used UAVs carring infrared and ordinary cameras to identify locations where delaminations exist in prefabricated beams. Kim *et al*. (2016) used airborne infrared thermal imaging to detect the facula of so lar panels in photovoltaic power plants with an accuracy of defective panels of 97%. Omar and Nehdi (2017) inspected concrete bridge decks using UAV infrared thermography. Biscarini *et al*. (2020) used UAV photogrammetry, infrared thermography and GPR for enhancing structural and material degradation evaluation. Cheng *et al*. (2019, 2020) proposed automatic delamination segmentation method for bridge deck through UAV-based thermography. Zhang *et al*. (2020) proposed an automatic detection method of earthquake-damaged buildings by integrating UAV oblique photography and infrared thermal imaging. However, the UAV-based thermography defect detection process usually generates large amounts of images. Therefore, developing a fast and intelligent image processing method to identify and quantify defect area with airborne imaging data is warranted.

As a rapidly developing method, the Deep Learning may be adopted to recognize a large amount of airborne imaging data. Recently, Janssens *et al*. (2018) applied specifically convolutional neural networks to determine the condition of the machine automatically by infrared thermal image. Gong *et al*. (2018) used deep learning approach for oriented electrical equipment detection in thermal images. Saeed *et al*. (2019) proposed an automatic defects detection method in CFRP thermograms using convolutional neural networks and transfer learning. Luo *et al*. (2019) established visual geometry group-Unet (VGG-Unet) for infrared thermal defect detection. Cheng *et al*. (2020) proposed an automatic delamination segmentation method for bridge deck based on encoder-decoder deep learning. These researches mainly focus on convolutional neural network to identify or quantify hidden defect by thermography images.

However, due to the infrared thermal image has uncleared edges and low pixel resolution, the pixel-level semantic segmentation networks applied on debonding defect recognition and quantification have two limitations: (1) the prediction mean or max area is quite different from the ground truth (Cheng *et al*. 2020); (2) a tremendous amount of time is required to build pixel-level data set (Kang *et al*. 2020). To address those problems, in this paper, we propose a debonding defect identification method of building decoration layers via UAV-thermography and point network CenterNet (Zhou *et al*. 2019), which is a single-stage detector with simple architecture and excellent detection performance. The infrared thermal videos of BDLs are acquired from an airborne videotape, based on a designed UAV flight route, and the usefulness of this method is shown in a case study of the old teaching-building detection to demonstrates the proposed framework in data acquisition, debonding defect thermography characteristics test and defect area quantification.

2. Methodology

In order to identify the debonding defects of BDLs, we have proposed a UAV-based thermography detection method, which is introduced in the following subsections. This framework involves three main tasks: (1) UAV system and data acquisition, (2) Experiment test of debonding defect thermography characteristics and (3) Deep learning-based defect recognition and quantification.

2.1 Thermography Image Data Acquisition

To achieve a higher resolution and photography scope, we have designed the UAV system and its inspection pattern. Then the thermal image data set of debonding BDLs are built for the further processing through a series of inspection based on a designed flight route UAV.


(a) UAV system

(b) Three-point laser rangefinder

(c) Operation system

(d) UAV in working state

Fig. 3 UAV-based Infrared thermography system

2.1.1 UAV system

The airborne infrared thermal inspection system is configured Fig. 3, which consists of a six-rotor UAV (1m in diameter and 0.8m in height), a GPS control system (for locating the real-time position of UAV), a wireless remote control system (for controlling the attitude of UAV and to planning a flight route), a DY640 infrared thermal imager (temperature resolution = 0.04 K, thermal sensitivity < 0.0350, image resolution = 640 × 480, and video frame rate = 25 frames per second), a lens with a focal length of 19 mm, and a three-point laser rangefinder with the ranging frequency adjustable to match the video frame rate (Zhong *et al*. 2018).

2.1.2 UAV Inspection patterns

(1) Data acquisition mode

There are two modes of image data acquisition based on the airborne infrared thermal imaging: photography and videotape. The airborne photography mode has advantages of clearer imaging and autonomous choice. But a qualified operator is required to operate the camera to capture suitable images. This procedure requires the take-off and landing repeatedly, which is time-consuming and relatively low automation level, while the airborne videotape mode could scan the entire area with a continuous and relatively smooth trajectory of flight, offering faster inspection speed and full coverage of inspection range. Therefore, we select the airborne videotape as the data acquisition mode of debonding defect inspection.

(2) UAV inspection route

The inspection route of UAV means designing a flight route that satisfies the intended mission requirements (Morgenthal *et al*. 2019). In this study, the commercial route plan system is used to design the UAV route and the laser range-finder is used to measure the distance between the UAV and BDLs in real time. In order to ensure the sufficient image resolution and the flight safety of UAV, the distance is set to be 6 m. The pixel resolution (J) at 6 m distance is calculated by Eq. (1).

$$J = L * \lambda = 6_m * 1.7_{\frac{m}{rad}} = 10.2\ \mathrm{mm/pixel} \qquad (1)$$

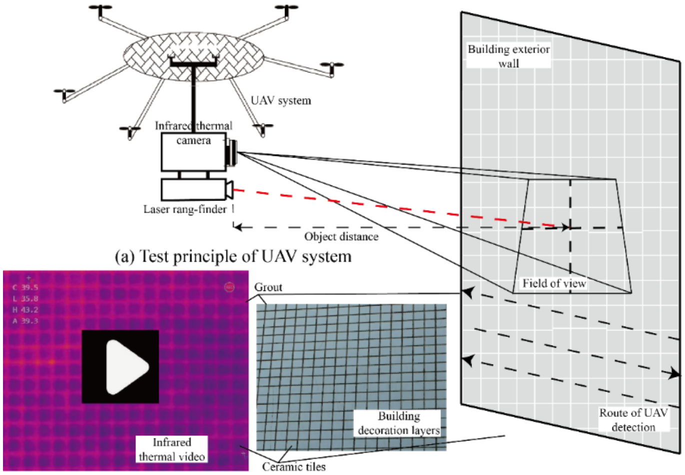

(a) Test principle of UAV system

(b) Test results by airbone thermography

Fig. 4 The detection process of UAV-based thermography

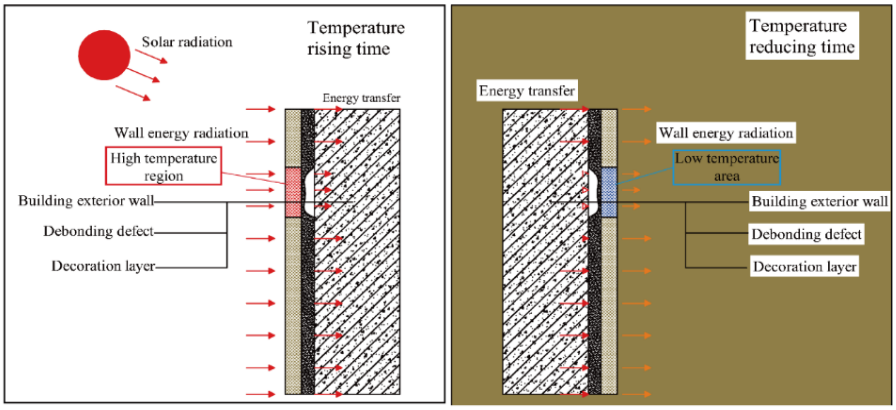

Fig. 5 The detection process of UAV-based thermography

$$V_{uav} = \frac{S_{pixel}}{t} = \frac{n \times J}{t} = 3 \times 0.0102 \times 25 \text{ m/s} = 0.765 \text{ m/s} \tag{2}$$

where L is the distance, and λ is the Instantaneous Field of View (IFOV). The airborne infrared video speed is 25 frames per second. According to reference (Li *et al*. 2018), the standard for airborne video clarity is that the displacement of the imaging point in single-frame is less than 3 pixels wide. In order to ensure no blur appearance, the flight speed of UAV is calculated, according to Eq. (2).

In Eq. (2), where V_{uav} is the speed of UAV, S_{pixel} is the minimum image shift, n is the minimum number of pixels, J is the resolution of pixels, and t is the time of single frame shooting. According to Eqs. (1) and (2), route schemes are planned under the distance of 6m and the flight speed of 0.6 m/s shown in Fig. 4.

2.2 Experiments study of debonding defect temperature field characteristics

Fig. 5 shows the energy radiation between the BDLs and the external wall. When the BDLs are debonding from the external wall, a thin air layer will be formed at the void position (Feng and Wang 2014). As the air has good thermal insulation, the heat transfer between the facing layer and building structure will be reduced. While, due to the solar shining, the temperature of external wall rises rapidly and conducts heat into the building interior. This results that the temperature of the debonding surface is higher than the normal positions. When the temperature drops, the debonding prevents the heat transfer from the building interior to the outer surface, making the debonding defect surface abnormally lower than the normal positions. According to this heat transfer law, the infrared thermal imaging image of debonding defect will be different from the normal positions, which can thus be used as the theoretical basis for identifying the debonding defect locations and areas.

2.2.1 Temperature field characteristics test of debonding defects under temperature change

In order to obtain temperature field characteristics of debonding defects, the experiments of debonding defects detection based on UAV thermography are carried out. The procedure mentioned above and the corresponding equipment are used for detection flight. The airborne infrared thermal video is decompressed frame by frame. Then, the images of debonding defects are arranged in typical time (Sunrise to sunset 8:00 am-18:00 pm) intervals shown in Fig. 6.

During the temperature-rising time from 8:00am to 14:00 pm, the temperature field of debonding area is abnormally higher than other locations. Contrarily, the temperature field of debonding area is lower than other positions from 14:00 pm to 18:00 pm. Especially at 10.00 am and 16:00 pm, the temperature field of debonding area is significantly higher or lower than other normal area because of the dramatic temperature change. Those results are consistent with the energy transfer principle of BDLs (Zhu *et al*. 2016). Based on these experiment results, the optimal inspection time is about 10:00 am shown in

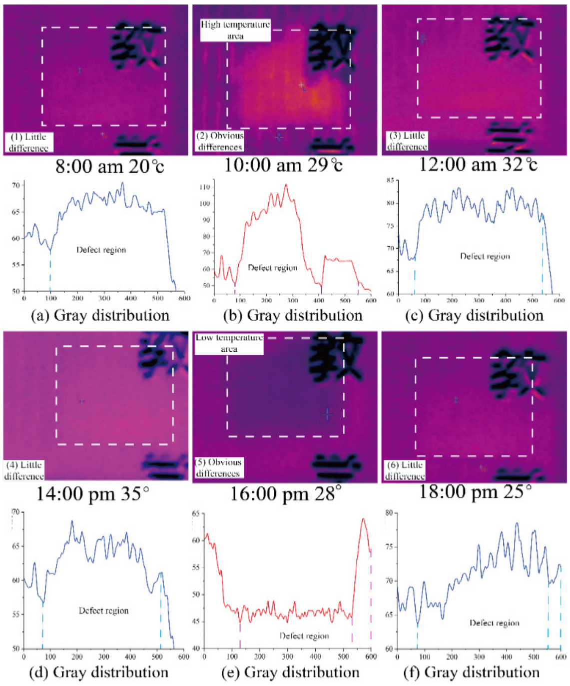

Fig. 6 Debonding defect's temperature field at different time

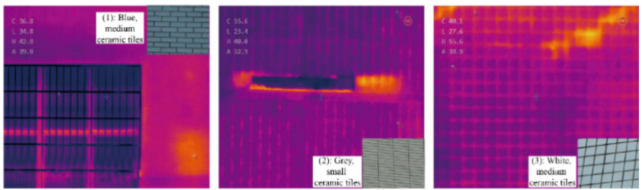

(a) Infrared images of different BDLs

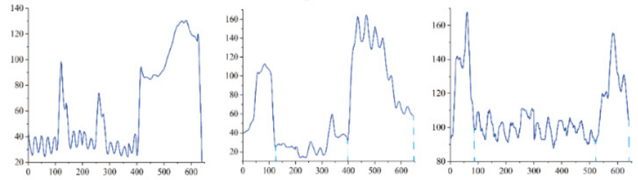

(b) Gray distribution of debonding defect

Fig. 7 Debonding defect's temperature field with different specifications

Fig. 6(b) because the infrared thermal image characteristics of defects in the temperature-rising stage are more prominent.

2.2.2 Temperature field characteristics test with different specifications

In order to obtain temperature field characteristics of debonding defects with different specifications, the debonding defects detection experiments are carried out in optimal inspection time. As shown in Fig. 7, the temperature fields of debonding areas are generally similar with different buildings, colours (blue, gray, white), specifications ceramic tile (25, 50, 75 square centimeters), indicating that the debonding defect recognition model trained by the same image data set is feasible. And the temperature field of debonding defects with different areas has a generally consistent gray gradient change from the center to the edge shown in Fig. 8. Meanwhile, the region-shape features of the grout and metal windows are different to those of the debonding defects showed in Fig. 7, which is hard to distinguish by traditional image processing method

2.3 The deep learning method of defect recognition

(a) Manual detection results

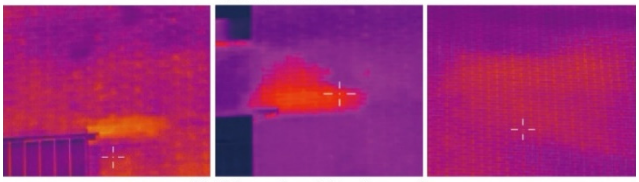

(b) IR image-based detection results

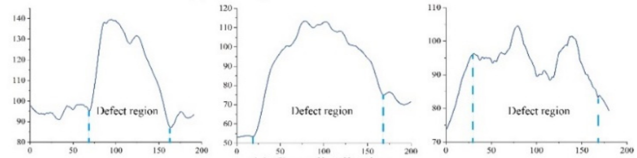

(c) Gray distribution

Fig. 8 Debonding defect's temperature field with different sizes

To quantify the debonding defect of BDLs based on UAV thermography videotape, we need classify and judge every pixel in an infrared thermal image as either "defect" or "non-defect". As shown in Fig. 9, there is an obvious heat source center in infrared image of the debonding defect, and the defect area has a gradient from defect center to the edge. Therefore, the debonding defect recognition method based on point network and fuzzy clustering is proposed shown in Fig. 10, and the recognition model is trained using images collected from the decompression infrared video frames of BDLs.

2.3.1 Centernet network

CenterNet (Zhou *et al*. 2019) is a single-stage detector with simple architecture and excellent detection performance. Compared with the traditional target detection model, it uses the center point to represent the anchor shown in Fig. 10, which solves the imbalance of positive and negative samples caused by the anchor. The center of the object's bounding box is modeled as a point object, and the center point is obtained by extracting the local peak points on the feature graph of key points, and then regressed to the object size and other attributes.

In the process of training, the standard intensive supervision is used to learn, each target only produces a center point, and the target position can be obtained without non maximum suppression. Compared with SSD, Yolo V3 and other real-time detection models, the CenterNet uses larger resolution output feature map for detection. And the CenterNet architecture can be divided into two parts: from bounding box to point and from point to bounding box, as shown in Fig. 10. The input image is extracted by ResNet network to get the output feature map, and then the target center point Y, the center point offset O and the target size S are trained respectively to realize the process from the

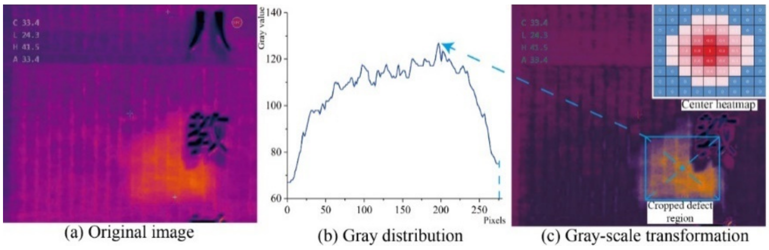

(a) Original image (b) Gray distribution (c) Gray-scale transformation

Fig. 9 Framework of debonding defect image process

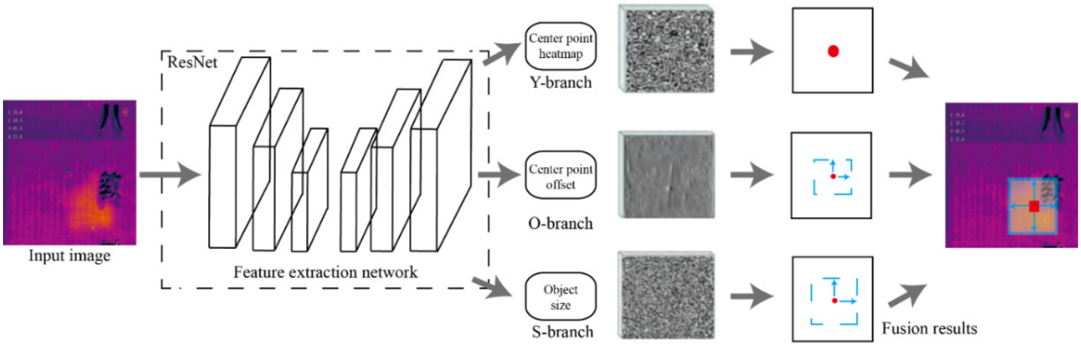

Fig. 10 CenterNet framework

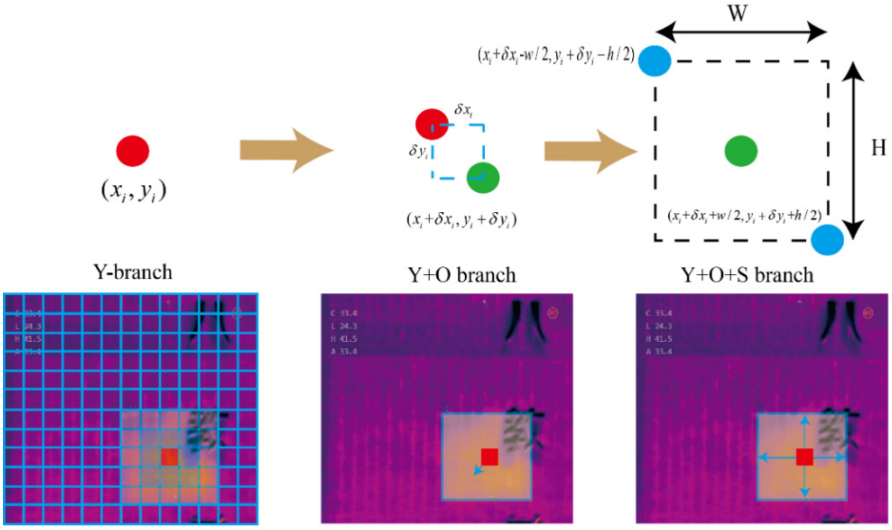

(a) Centre point of target (b) Offset of centre-point (c) Range of object

Fig. 11 Process of from point to bounding box

boundary frame to the point. Then, the training results of Y, O and S branches are decoded into the object bounding box to realize the transformation from point to bounding box.

(1) From bounding box to point

The process of that from bounding box to point is shown in Fig. 10. The labeled image is input into the feature extraction network to get the output feature map. Then, the key point prediction Y branch, the center deviation O branch and the object size S branch share the same feature extraction network for training respectively. Finally, the whole network predicts 84 values of the center point position of each object, namely, the key point predicts of Y branch results, the O branch result x and y of the center point deviation, and the result of the object size branch w and h.

In the key point prediction Y branch, the image $I \in R^{W \times H \times 3}$ is input into the feature extraction network of centernet to generate the key point heat-map $Y \in [0,1]^{\frac{W}{4} \times \frac{H}{4} \times 80}$, namely Gaussian distribution map. Among them, the peak in the distribution map corresponds to the center of the object, 4 refers to the scale of the output size, and 80 refers to the number of channels in the output feature map. When training the key point prediction network, for each real frame key of c class, first calculate low resolution equal value, and then use Gaussian kernel to map the key points of each real frame to the heatmap $Y \in [0,1]^{\frac{W}{4} \times \frac{H}{4} \times 80}$. In the center point offset O branch, the local offset of each center point is to use L1 loss to train the offset value of all objects' center points. All similar objects share a predicted offset value to recover the discretization error caused by output step length. In the dimension S branch, the width height of the object is regressed at the target center position, and $(x_1^{(k)}, y_1^{(k)}, x_2^{(k)}, y_2^{(k)})$ is the boundary box of target k.

(2) From point to bounding box

The process of that from point to bounding box is similar to decoding shown in Fig. 11. Let $p = \{(x_i, y_i)\}_{i=1}^{n}$ be the set of n center points of class C detected. The boundary box is obtained by extracting 100 peak points of each category on the thermal graph. If the peak points are larger than 8 neighborhood points, the boundary box is retained. The key points Y, deviation O and dimensions S predicted by the model are generated at the designated position. This method can improve the performance of the model by directly estimating the key points.

The steps of generating the bounding box are shown in

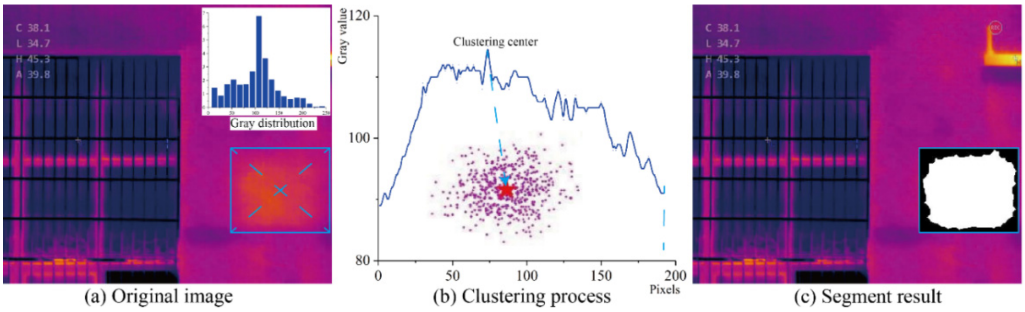

(a) Original image (b) Clustering process (c) Segment result

Fig. 12 Process of image fuzzy clustering

Fig. 11. $(x_i, y_i) = Y_{xiyi80}$ is the position of the prediction center point, $(\delta x_i,\ \delta y_i)$ is the offset prediction result, and (W, H) is the predicted target width and height information. In the process of generating the bounding box, the center point predicted by the model is obtained first, and then the offset is added to get the offset center point. Finally, the target bounding box is generated by adding the center point and the size of training object.

2.3.2 Fuzzy clustering method

Clustering is the process of clustering some sample data with the same characteristics to realize the classification of sample data. The infrared image segmentation based on fuzzy clustering uses the center point identified by the point network as the clustering center. The minimum value of the target function is calculated by the membership relationship between the pixels and the center in the region to separate the fuzzy boundary of the infrared image and segment the defect region image at the pixel level (Wang *et al*. 2020). The objective function of the algorithm is shown Eq. (3)

$$J = \sum_{i=1}^{n}\sum_{k=1}^{c} u_{ik}^{m}\,(X_i - X_K)^2 \tag{3}$$

Where n is the number of pixels, c is the number of clustering centers, u is the membership degree relative to class k, m is the fuzzy weight coefficient, X_i is the pixel gray level, and X_k is the clustering center. The constraints of membership degree u are as follows

$$\sum_{k=1}^{c} u_{ik}^{m} = 1, \quad \forall_i = 1,2,3\ldots,n \tag{4}$$

Therefore, the clustering problem becomes a nonlinear optimization, and the minimum value of the objective function under the constraint Eq. (4) is solved. By introducing Lagrange multiplier, the equation is transformed into the following

$$J = \sum_{i=1}^{n}\sum_{k=1}^{c} u_{ik}^{m}\,(X_i - X_K)^2 + \sum_{i=1}^{n} \lambda_i\,(1 - \sum_{k=1}^{c} u_{ik}) \tag{5}$$

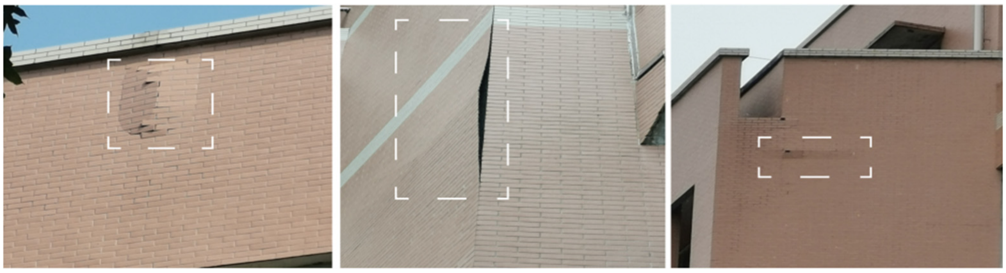

(a) Examples of BDLs deponding defect

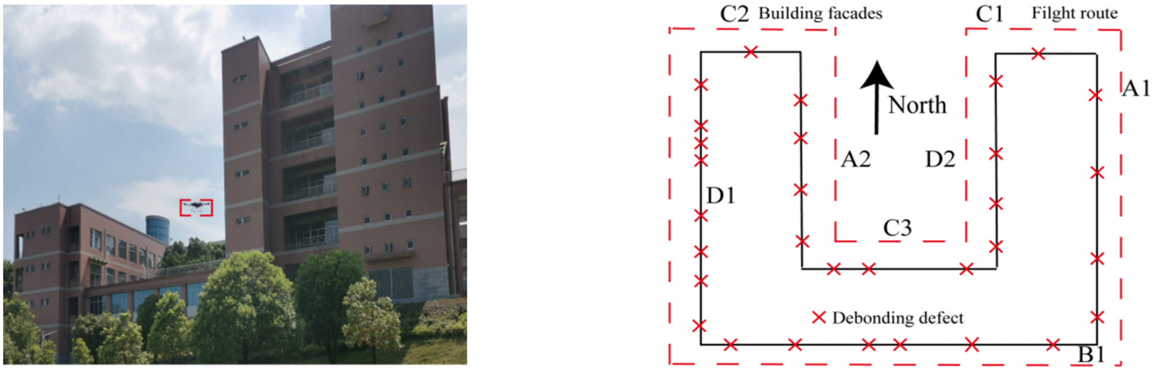

(b) Inspection process based on UAV (c) Inspection route and results of tested building

Fig. 13 Process of image fuzzy clustering

Due to the debonding defect has the characteristics of abnormally high temperature field during the heating period, the fuzzy clustering algorithm is used to segment the thermal imaging image. The steps are as follows: calculating the gray histogram of cropped region, as shown in Figs. 12(a) and (b); (2) determining the number of clustering categories as 2 according to the gray histogram; (3) calculating the gray histogram objective function Eq. (3). If the objective function is smaller than a certain threshold range the algorithm stops; (4) use Eq. (4) to generate the new fuzzy matrix U, and then return to step (3). So as to determine the center of all kinds of clustering and the membership matrix of all kinds of sample data, and complete the clustering segmentation, as shown in Fig. 12(c).

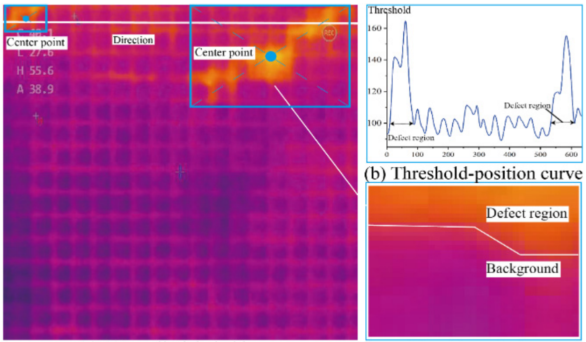

(a) Manually labeled image (b) Threshold-position curve (c) Enlarged edge

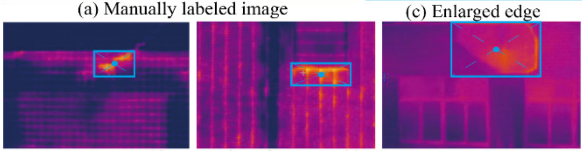

(d) Examples of annotated image

Fig. 14 Examples of manually labeled images

3. Case study

As shown in Fig. 13, the proposed method and system are applied on an old teaching-building located at the authors' institution to detect debonding defect of BDLs. Similarly, the traditional method using artificial harmer is also applied to verify the detection accuracy of the proposed method. According to the facade orientation of this building, the flight inspection route is planned from the East to the West. The detected debonding defect and its parameters of GPS positioning coordinates, and the real-time distance measured by the three-point laser rangefinder is obtained, as marked in the Fig. 13(c). The physical size of the thermal sensor in the camera was 640 × 480 pixels. During inspection, the operator controls the UAV system at a low speed of 0.6 m/s, and it takes approximately 2 hours to cover the entire inspection area listed in Table 1.

3.2 Model training and validation

3.2.1 Image data annotation

To achieve a good performance, we select approximately 1000 images from the airborne infrared thermal videos of BDLs and annotated by a graphical image annotation tool named labelImg to form an image data set. As shown in Figs. 14(a), (b), (c), all the images are annotated with ground-truth bounding boxes and class labels using labelImg. According to the grayscale difference of debonding areas, the debonding defects region are marked in a bounding box, as shown in Fig. 14(d). The size of the labelled image is 640 pixel × 480 pixels, forming a total of 1000 image sample data sets. As shown in Table 2, according to the ratio of the training set to verification set = of 4:1, the image sample data are divided into the training set and verification set.

3.2.2 Model training and evalution

(1) Training

The CenterNet network are trained by above data sets of debonding defects to generate the semantic segmentation model. The hardware system used in training is Intel core i7-7700@ 3.60 GHz 8 core processor with 64 GB running memory (RAM) and it is accelerated by NVIDIA Geforce

Table 1 Information of system implementation experiments

Items	Façade orientation	Inspection start time	Flight time	Defect numbers
Flight route A	East	10:00 am	20 + 15 min	18
Flight route B	South	11:00 am	22 min	16
Flight route C	North	11:20 am	10 + 10 + 12 min	15
Flight route D	West	13:00 pm	20 + 15 min	22

Table 2 Debonding defects image data set

Items	No. of images	Size (pixels)	Defect	Training	Validation
Defect with window noise	327	640×480	327	261	66
Defect with grout noise	262	640×480	262	210	52
Defect with other noise	226	640×480	226	181	45
Defect with no noise	185	640×480	185	148	37
Total	1000	640×480	1000	800	200

Table 3 Model evaluation

Items	Defect image	Defect image with noise	Total
Training	148	652	800
Validation	37	163	200
Average IoU	94.36	91.27	92.04

GTX-1080Ti graphics card, with running in Pytorch framework under Linux Ubuntu system. Once the loss of the CenterNet network in the training process decreases to stable, indicating that the recognition model is trained and suitable for identify the debonding defect images.

(2) Evaluation

In a further attempt to evaluate the segmentation model, the images of the test set are input into the trained CenterNet model and fuzzy clustering algorithm. The predicted results are compared with the ground-truth using statistical indicator, IoU (Intersection over Union) to evaluate the model. IoU is defined as (Yu *et al*. 2016)

$$IoU = \frac{TP}{TP + FP + FN} \tag{6}$$

where TP and FP are the positive and negative samples predicted by the model respectively and FN is a positive sample predicted to be negative by the model. The result of the model evaluation is shown in Table 3, indicating that the proposed method could attain more than 92% precision.

3.3 Recognition results and area quantification

3.3.1 Recognition results

This trained CenterNet network model processes an input image and produces an output image with the same size. As shown in Figs. 15 and 16, the defect image with hot window and grout noise is extracted through the trained model. All the debonding defects in the test image data set are recognized with an accuracy almost equal to the ground-truth by the proposed model, while the traditional image processing methods need to adjust the segmentation threshold and interfered by noise (such as: window, grout) easily. The prediction results show that the proposed method has good robustness and generalization ability for debonding defect images with low contrast, blurred edge, and the interference of pseudo-features.

3.3.2 Quantification of debonding defect area

To assess the debonding defect quantificationally, the debonding defect area of the image was calculated by counting the pixel area with the application of toolbox. Afterwards, the actual defect areas are calculated through the optical imaging principle by Eq. (1) from the real-time distance data obtained by synchronized three-point laser rangefinder. In Fig. 17, results show that the proposed method can accurately (≥ 90%) identify and quantify the defect area and location.

3.4 detection results and analysis

As listed in Table 1, eight videos are recorded during the detection and decompressed to images frame by frame. Then the images are imputed to the trained model for identifying the defect area. To determine the accuracy of the debonding defect recognition using the proposed method, the traditional manually identification for each defect area is conducted as a reference. Following this, total 71 regions are identified as debonding defect and its actual areas are calculated accurately by the Eq. (1). To be specific, several sample frames are provided as shown in Fig. 17. It can be recognized as a high accuracy above 90% when the defect area is larger than 30 cm × 10 cm. Result of the proposed method shows that approximately 98% of the defect area are completely identified while only 2% of the images are missed identified. The reason why some area is missed as identified is because they are too small (≦ 300 square centimeters). It means that dangerous parts defect can be identified effectively.

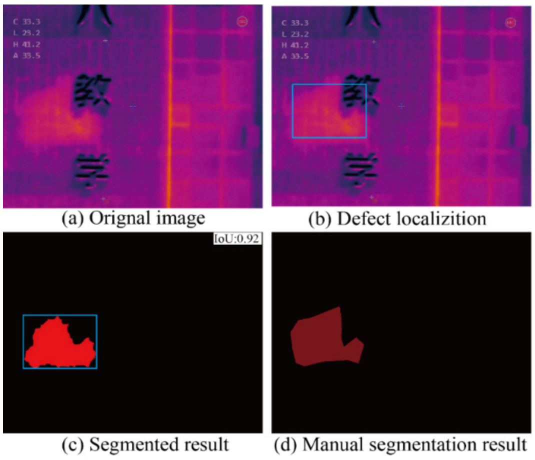

Fig. 15 Example of defect recognition with hot window noise

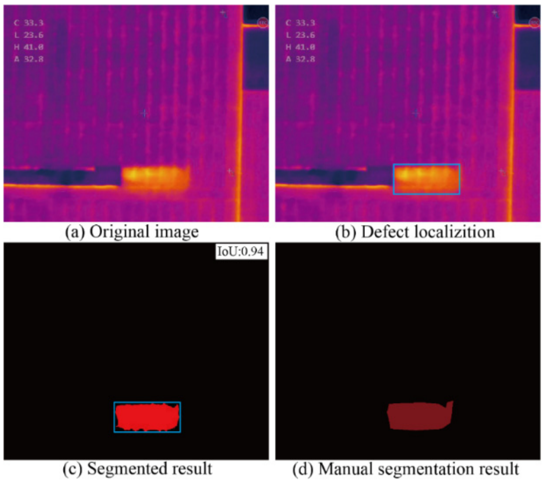

Fig. 16 Example of defect recognition with hot grout noise

(a)Manual detection result

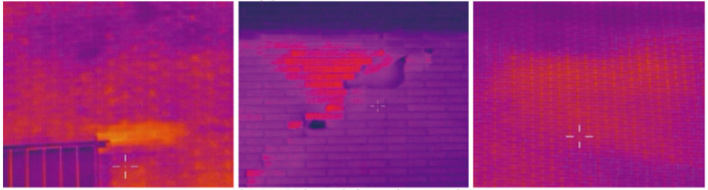

(b) UAV-based detection results

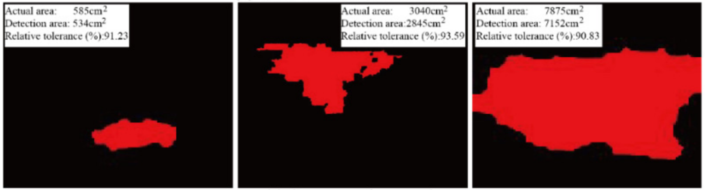

(c) Segmentation results

Fig. 17 Examples of debonding defect inspection result

4. Discussion

Results presented in this paper demonstrate that the proposed method based on UAV thermography is capable to estimating the debonding defect area quantificationally, allowing the isolation of debonding defect from noise which had not been realized in previous research. It produces a pixel-level segmentation result, providing an increased detectability of the potential threatens on the building exterior wall by using use infrared thermal videos as input and to produce labeled images as output. The deep learning algorithm is also more automatically and rapidly than traditional method in the case studies. However, this method is still influenced by some factors caused by environment or equipment, as discussed below.

4.1 Influence factors

4.1.1 Temperature

According to the references, the most essential issue for temperate field characteristic is the change of solar radiation in the natural environment. As shown in Fig. 18, the previously mentioned experiments have verified that the optimal inspection time given in this paper is approximately 10:00 am in summer along with the faster temperature change, which would generate the most significant boundary between the normal and abnormal area. However, the specific optimal time of this method may be decided by weather, seasons, wind speed and so on. As shown in Fig. 18, the temperature change curve of westward, southward and northward BDLs is slightly different, so that the BDLs inspection should be carried out in the time that one or two hours later after the recommended time depending on the weather conditions. Despite having relatively large impact, the aforementioned method still present good robustness using the deep learning algorithm, which can identify the defects with low contrast, blurred edge, and the interference of pseudo-features automatically achieving above 90% accuracy.

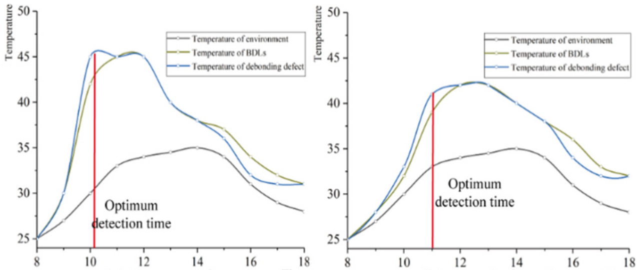

(a) Eastern facade (b) South facade

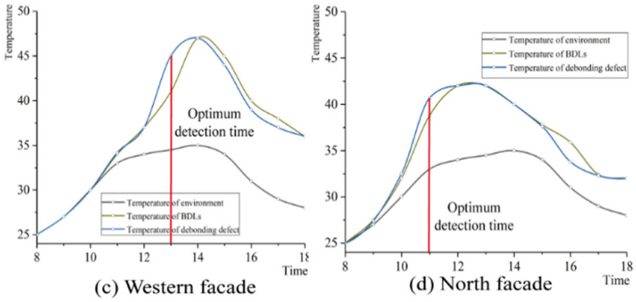

(c) Western facade (d) North facade

Fig. 18 The optimum inspection time of different building facade

4.1.2 Strong heat source

When the proposed method is applied in the inspection of building exterior wall, the infrared characteristic of defect area often be interfered by the heat source, such as window, door, air-conditioning and so-on because that they are metal materials heating up more easily under the solar radiation. If there are small size defect near the strong heat source, its boundary between the defect and heat source object will become blurred providing an increased difficulty on identifying the real defect.

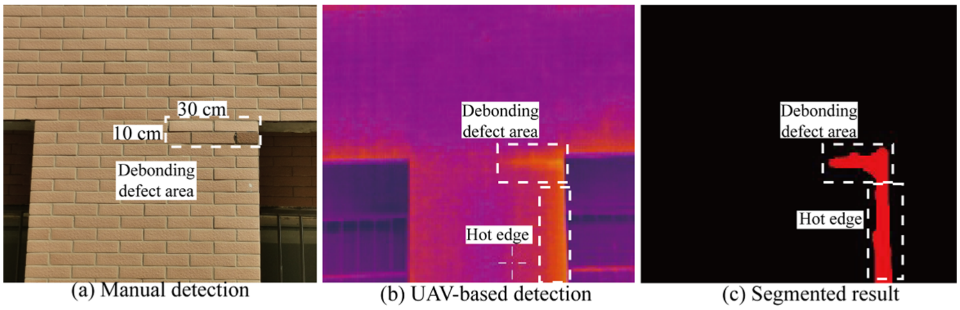

(a) Manual detection (b) UAV-based detection (c) Segmented result

Fig. 19 Example of defect infrared image influenced by strong heat source

As shown in Fig. 19, the original image, infrared thermal image and the segmented image are listed. After the image processing based on the proposed method, its recognition result is enlarged since it is influenced by the strong heat source, which will bring a huge error to the inspection results. Compared with the manual recognition result, the inspection result has been amplified more than doubled. Consequently, this situation should be recognized by combining the deep learning algorithm and traditional image processing method, which will improve the accuracy of debonding defect inspection. In this sample, the recognition accuracy can reach 82% through manual intervention.

4.2 Limitation and further study

The proposed method also has some limitations. First, although the proposed method is less difficult in recognizing the defect area than the traditional method, it is still a post-hoc analysis system. Second, the processing object is video in this method rather than images, it also needs large amounts of annotated images to train the network producing manual work. Besides, building forms are often complicated, and there possibly have inspection errors or omissions in UAV routes planned by a single path. Therefore, the separate flight route planning is required for connection systems or complex building facade inspection. To ensure the safety of UAVs, the skilled operators should monitor the status of UAVs from time to time to avoid dangerous situations. In the future, with real-time video processing capability, the proposed system can be installed to the UAV platform, which can facilitate the on-site operator in the video collection process. A special analysis software for real-time inspection with airborne thermal imaging system may be designed in the future.

5. Conclusions

In this paper, we have developed a UAV-based thermography method for BDL's debonding defect detection and quantification. Based on this study, the following major findings are offered:

- At first, we have tested the temperature field characteristics of debonding defects under different environmental temperature and different temperature changes. Through these time series experiments, the heat transfer law of the BDLs in the relevant references is verified, and the optimal debonding defect detection time is determined. Also, we have found that the temperature field characteristics of the debonding defects have little relationship with the finishing materials, sizes and BDL colors, and the debonding defects of BDLs have obvious shape differences with other heat sources, such as windows, grout and so on, which lays the foundation for the automatic recognition and analysis method based on infrared imaging.
- We have proposed a debonding defect recognition and quantification method combining CenterNet and fuzzy clustering. Although the infrared thermal image of debonding defect have uncleared edges and low pixel resolution. In this method, debonding defect area and its center point can be detected by CenterNet network, and bridge crack can be segmented in pixel-level with high-accuracy based on fuzzy clustering, which has the advantages of simple sample making, reliable and stable results, and high generalization ability. Finally, the case study of the old teaching-building inspection has been carried out to demonstrate the effectiveness of the proposed method. Compared with the manual detection results, the accuracy of proposed bridge crack width recognition method is more than 90%, showing good reliability to debonding defect detection and evaluation.
- According to the study results, it is suggested that the debonding defect inspection should be implemented during the periods of dramatic temperature rise in summer or autumn.

Acknowledgments

This study is supported by National Natural Science Foundation of China (Grant No. 51678235), to which the authors are grateful.

References

Bang, H.T., Park, S. and Jeon, H. (2020), "Defect identification in composite materials thermography and deep learning techniques", *Compos. Struct.*, **246**, 112405. https://doi.org/10.1016/j.compstruct.2020.112405

Biscarini, C., Catapano, I., Cavalagli, N., Ludeno, G., Pepe, F.A. and Ubertini, F. (2020), "UAV photogrammetry, infrared thermography and GPR for enhancing structural and material degradation evaluation of the Roman masonry bridge of Ponte Lucano in Italy", *NDT & E Int.*, **115**, 102287. https://doi.org/10.1016/j.ndteint.2020.102287

Cheng, C., Shang, Z. and Shen, Z. (2019), "Bridge deck delamination segmentation based on aerial thermography through regularized grayscale morphological reconstruction and gradient statistics", *Infrared Phys. Technol.*, **98**, 240-249. https://doi.org/10.1016/j.infrared.2019.03.018

Cheng, C., Shang, Z. and Shen, Z. (2020), "Automatic delamination segmentation for bridge deck based on encoder-decoder deep learning through UAV-based thermography", *NDT & E Int.*, **116**, 102341. https://doi.org/10.1016/j.ndteint.2020.102341

Cotič, P., Kolarič, D., Bosiljkov, V.B., Bosiljkov, V. and Jagličić, Z. (2015), "Determination of the applicability and limits of void and delamination detection in concrete structures using infrared thermography", *NDT & E Int.*, **74**, 87-93. https://doi.org/10.1016/j.ndteint.2015.05.003

Ellenberg, A., Kontsos, A., Moon, F. and Bartoli, I. (2016), "Bridge deck delamination identification from unmanned aerial vehicle infrared thermography", *Automat. Constr.*, **72**, 155-165. https://doi.org/10.1016/j.autcon.2016.08.024

Feng, L. and Wang, H. (2014), "Experimental Study on Inside Defects of Building Exterior Wall Decoration Layer by Infrared Thermal Imaging Method", *J. Chongqing Jianzhu Univ. China*, **36**(2), 57-61.

Gong, X., Yao, Q., Wang, M. and Lin, Y. (2018), "A deep learning approach for oriented electrical equipment detection in thermal images", *IEEE Access*, **6**, 41590-41597. https://doi.org/10.1109/ACCESS.2018.2859048

Hwang, S., An, Y.K., Yang, J. and Sohn, H. (2020), "Remote inspection of internal delamination in wind turbine blades using continuous line laser scanning thermography", *Int. J. Precis. Eng. Manuf.-Green Technol.*, 1-14. https://doi.org/10.1007/s40684-020-00192-9

Jang, K., Kim, N. and An, Y.K. (2019), "Deep learning–based autonomous concrete crack evaluation through hybrid image scanning", *Struct. Health Monitor.*, **18**(5-6), 1722-1737. https://doi.org/10.1177/1475921718821719

Jang, K., An, Y.K., Kim, B. and Cho, S. (2021), "Automated crack evaluation of a high-rise bridge pier using a ring-type climbing robot", *Comput.-Aided Civil Infrastruct. Eng.*, **36**, 14-29. https://doi.org/10.1111/mice.12550

Janssens, O., Van de Walle, R., Loccufier, M. and Van Hoecke, S. (2018), "Deep learning for infrared thermal image based machine health monitoring", *IEEE/ASME Transact. Mechatron.*, **23**(1), 151-159. https://doi.org/10.1109/TMECH.2017.2722479

Jung, H.J., Lee, J.H., Yoon, S. and Kim, I.H. (2019), "Bridge Inspection and condition assessment using Unmanned Aerial Vehicles (UAVs): Major challenges and solutions from a practical perspective", *Smart Struct. Syst.*, *Int. J.*, **24**(5), 669-681. https://doi.org/10.12989/sss.2019.24.5.669

Kang, D., Benipal, S.S., Gopal, D.L. and Cha, Y.J. (2020), "Hybrid pixel-level concrete crack segmentation and quantification across complex backgrounds using deep learning", *Automat. Constr.*, **118**, 103291. https://doi.org/10.1016/j.autcon.2020.103291

Kim, D., Youn, J. and Kim, C. (2016), "Automatic photovoltaic panel area extraction from uav thermal infrared images", *J. Korean Soc. Survey. Geodesy Photogram. Cartogr.*, **34**(6), 559-568.

Kim, H., Lee, J., Ahn, E., Cho, S., Shin, M. and Sim, S.H. (2017), "Concrete crack identification using a UAV incorporating hybrid image processing", *Sensors*, **17**(9), 2052. https://doi.org/10.3390/s17092052

Li, K., Wang, X., Guo, B., Liu, H., and Yuan, H. (2018), "Dynamic simulation of imaging blurring effect of infrared system under vibration of carrier platform", *Infrared Laser Eng. China*, **47**(09), 83-88. https://doi.org/10.3788/IRLA201847.0904004

Liu, P., Chen, A.Y., Huang, Y.N., Han, J.Y., Lai, J.S., Kang, S.C., Wu, T.H., Wen, M.C. and Tsai, M.H. (2014), "A review of rotorcraft Unmanned Aerial Vehicle (UAV) developments and applications in civil engineering", *Smart Struct. Syst.*, *Int. J.*, **13**(6), 1065-1094. http://dx.doi.org/10.12989/sss.2014.13.6.1065

Luo, Q., Gao, B., Woo, W.L. and Yang, Y. (2019), "Temporal and spatial deep learning network for infrared thermal defect detection", *NDT & E Int.*, **108**, 102164. https://doi.org/10.1016/j.ndteint.2019.102164

Morgenthal, G., Hallermann, N., Kersten, J., Taraben, J., Debus, P., Helmrich, M. and Rodehorst, V. (2019), "Framework for automated UAS-based structural condition assessment of bridges", *Automat. Constr.*, **97**, 77-95. https://doi.org/10.1016/j.autcon.2018.10.006

Omar, T. and Nehdi, M.L. (2017), "Remote sensing of concrete bridge decks using unmanned aerial vehicle infrared thermography", *Automat. Constr.*, **83**, 360-371. https://doi.org/10.1016/j.autcon.2017.06.024

Özcan, O. and Özcan, O. (2021), "Automated UAV based multi-hazard assessment system for bridges crossing seasonal rivers", *Smart Struct. Syst.*, *Int. J.*, **27**(1), 35-52. https://doi.org/10.12989/sss.2021.27.1.035

Pitarma, R., Crisóstomo, J. and Pereira, L. (2019), "Detection of wood damages using infrared thermography", *Procedia Comput. Sci.*, **155**, 480-486. https://doi.org/10.1016/j.procs.2019.08.067

Rocha, J.H.A., Póvoas, Y.V. and Santos, C.F. (2019), "Detection of delaminations in sunlight-unexposed concrete elements of bridges using infrared thermography", *J. Nondestr. Eval.*, **38**(1), 1-12. https://doi.org/10.1007/s10921-018-0546-5

Saeed, N., King, N., Said, Z. and Omar, M.A. (2019), "Automatic defects detection in CFRP thermograms, using convolutional neural networks and transfer learning", *Infrared Phys. Technol.*, **102**, 103048. https://doi.org/10.1016/j.infrared.2019.103048

Sirca Jr, G.F. and Adeli, H. (2018), "Infrared thermography for detecting defects in concrete structures", *J. Civil Eng. Manage.*, **24**, 508-515.

Wang, X., Hu, F. and Huang, S. (2020), "Infrared image segmentation algorithm based on distribution information intuitionistic fuzzy c-means clustering", *J. Commun. China*, **41**(5), 120-129.

Yu, J., Jiang, Y., Wang, Z., Cao, Z. and Huang, T. (2016), "Unitbox: An advanced object detection network", *Proceedings of the 24th ACM International Conference on Multimedia*, pp. 516-520.

Zhang, X., Li, C., Meng, Q., Liu, S., Zhang, Y. and Wang, J. (2018), "Infrared image super resolution by combining compressive sensing and deep learning", *Sensors*, **18**(8), 2587. https://doi.org/10.3390/s18082587

Zhang, R., Li, H., Duan, K., You, S., Liu, K., Wang, F. and Hu, Y. (2020), "Automatic detection of earthquake-damaged buildings by integrating UAV oblique photography and infrared thermal imaging", *Remote Sens.*, **12**(16), 2621. https://doi.org/10.3390/rs12162621

Zhong, X., Peng, X., Yan, S., Shen, M. and Zhai, Y. (2018), "Assessment of the feasibility of detecting concrete cracks in images acquired by unmanned aerial vehicles", *Automat. Constr.*, **89**, 49-57. https://doi.org/10.1016/j.autcon.2018.01.005

Zhou, X., Wang, D. and Krähenbühl, P. (2019), "Objects as Points", arXiv:1904.07850.

Zhu, H., Yi, C., Hu, Y. and Liu, Q. (2016), "Study on Detection

Conditions for Infrared Thermography Diagnosis of Debonding Defect of Exterior Wall Decoration Layer", *Build. Technol. China*, **47**(2), 172-175.

HJ